Nano Energy 72 (2020) 104689

Contents lists available at ScienceDirect

Nano Energy

journal homepage: http://www.elsevier.com/locate/nanoen

Full paper

Solution-processable two-dimensional ultrathin nanosheets induced by self-assembling geometrically-matched alkane

Dan Luo [a,1,*], Boyang Zhou [a,g,1], Bowen Guo [a], Peng Gao [e], Lei Zheng [f], Xiaojun Zhang [a], Shengjie Cui [b,d], Hongjun Zhou [a], Yongsheng Zhou [c,d,**], Yan Liu [b,d,***]

[a] State Key Laboratory of Heavy Oil Processing, College of New Energy and Materials, Beijing Key Laboratory of Biogas Upgrading Utilization, China University of Petroleum (Beijing), Beijing, 102249, China
[b] Laboratory of Biomimetic Nanomaterials, Department of Orthodontics, Peking University School and Hospital of Stomatology, Beijing, 100081, China
[c] Department of Prosthodontics, Peking University School and Hospital of Stomatology, Beijing, 100081, China
[d] National Engineering Laboratory for Digital and Material Technology of Stomatology, National Clinical Research Center for Oral Diseases, Beijing Key Laboratory of Digital Stomatology, Beijing, 100081, China
[e] Electron Microscopy Laboratory, School of Physics, Peking University, Beijing, 100871, China
[f] Institute of High Energy Physics, Chinese Academy of Sciences, Beijing, 100049, China
[g] Graduate School of Energy Science, Kyoto University, Yoshida-honmachi, Sakyoku, Kyoto, 606-8501, Japan

ARTICLE INFO

Keywords:
Two-dimensional nanomaterials
Solution-processable
Self-assembly
Geometrically-matched alkane
Photoelectrochemical application

ABSTRACT

Two-dimensional (2D) nanomaterials have attracted much interest as promising candidates for next generation energy storage, electronics and catalytic applications, due to their unique topology and electronic structure. However, the development of an operable and versatile solution processing technique for simple fabrication of high-quality 2D nanosheets continues to present a significant challenge. Here, an ultrathin indium sulfide nanosheet is synthesized via a simple solution-phase reaction involving two steps: i) thermal decomposition of precursors to form a crystal nucleus; ii) growth of 2D nanosheets in a mixture of amino ligand and alkane solvent. The alkane, matching the amino ligand structure in terms of geometry, could assemble with the ligand to form a soft template and thus induce a 2D arrangement of the nucleus. Moreover, the chemical inertness of the alkane facilitated rotation of crystal seeds, resulting in anisotropic growth of the nanosheet. We further demonstrated that the geometrically matched alkane-assisted solution processing reaction could be applied to synthesize various 2D metal chalcogenides. Functionally, the acquired indium sulfide nanosheets, which possess high photoelectric activity, were introduced for fabrication of photoelectrodes capable of efficient photoelectrochemical water splitting. Our work opens up a new perspective toward the construction and potential applications for various 2D nanomaterials.

1. Introduction

Two-dimensional (2D) materials, composed of atomic-scale crystal layers, have been studied extensively due to their special structures and a wide variety of unusual physical phenomena [1–6]. Due to quantum confinement of carriers, attributable to their extraordinarily small dimensions in thickness, 2D materials exhibit the quantum spin Hall effect [7,8], the quantum anomalous Hall effect [9], valley polarization and superconductivity [6,10–12], and hence have great potential for applications in energy storage devices, topological insulators and field effect transistors [13–19]. Moreover, the highly exposed surface atoms of 2D nanomaterials endow them with increased chemical activity, which is favorable for electrocatalysis, photocatalysis and heterogeneous catalysis [20–33]. So far strategies such as template growth method,

* Corresponding author. State Key Laboratory of Heavy Oil Processing, College of New Energy and Materials, Beijing Key Laboratory of Biogas Upgrading Utilization, China University of Petroleum (Beijing), Beijing, 102249, China.
** Corresponding author. Department of Prosthodontics, Peking University School and Hospital of Stomatology, Beijing, 100081, China.
*** Corresponding author. Laboratory of Biomimetic Nanomaterials, Department of Orthodontics, Peking University School and Hospital of Stomatology, Beijing, 100081, China.
E-mail addresses: luodan@cup.edu.cn (D. Luo), kqzhouysh@hsc.pku.edu.cn (Y. Zhou), orthoyan@bjmu.edu.cn (Y. Liu).
[1] These authors have contributed equally.

https://doi.org/10.1016/j.nanoen.2020.104689
Received 12 February 2020; Received in revised form 6 March 2020; Accepted 9 March 2020
Available online 17 March 2020

mechanical and chemical exfoliation and chemical vapor deposition have been successfully applied for the synthesis of 2D nanomaterials [34–40]; however, a versatile method for fabricating a broad portfolio of 2D materials with diverse chemical compositions is still lacking. Although a library of 2D transition-metal chalcogenides have been produced recently via a universal salt-assisted chemical vapor deposition method, relatively harsh experimental conditions as well as difficulties in the transfer process, limit their wide applications [41].

Liquid phase reaction is an effective method for fabricating nanostructures on a large scale. In general, the growth of anisotropic structures often relies on the use of templates; to facilitate separation and purification of nanostructures, an easily accessible and removable template is often required. Here, we synthesized metal chalcogenide ultrathin nanosheets by developing a general and simple solution processing approach, in which a soft template was formed via integrated assembly of amino ligands (octylamine) and alkane solvent molecules (octane), inducing anisotropic growth of nanosheets. During the reaction process, the chemical inertness and stoichiometry of the alkane determines the nanotopography of the materials, and single-crystalline indium sulfide (In_2S_3) nanosheets with a narrow thickness range could be obtained successfully under a highly concentrated alkane atmosphere, with an alkane, geometry that matches the amino ligand. Our geometrically matched alkane-assisted solution processing strategy was also applied to synthesize other metal chalcogenide 2D nanosheets, including Co_9S_8, MoS_2, Al_2S_3, SnS_2 and MnS. The acquired In_2S_3 nanosheets, which showed high photoelectric activity, served as a versatile platform for multi-functional photoelectrochemical (PEC) applications after loading various catalytic components. This work provides a new perspective on the fabrication of solution-processable 2D materials, and offers tremendous potential for future design of 2D material-based heterostructure devices.

2. Experimental section

2.1. Synthesis of In_2S_3 ultrathin nanosheets

The nanosheets were synthesized via a simple solution-phase reaction involving two steps: i) thermal decomposition of precursors to form a crystal nucleus; and ii) growth of 2D nanosheets in a mixture of amino ligand and alkane solvent. By simply altering the chemical composition and stoichiometry of the metal precursor, different nanosheets were formed. Specifically, 0.2 mM indium acetate, 0.3 mM sulfur powder and 16 mL octylamine/octane mixed solution (2%: 98%) were added into glass round bottom flask. After ultrasonic mixing, the mixture was transferred into a PPL-lined stainless-steel autoclave, and then heated to 250 °C for 12 h. The reaction was stopped by rapid water cooling to room temperature, and the acquired nanosheets were washed five times by adding appropriate amount of ethanol.

2.2. Characterization

The morphology of nanosheets was examined by TEM (JEOL Ltd., JEM2011) at 100 kV. The HRTEM was performed on a Field Emission Transmission Electron Microscope (JEOL Ltd., JEM-2100F) at 200 kV. To identify the atomic structure of ultrathin nanosheets, high-resolution quantitative STEM images and high-angle annular dark-field (HAADF) images were acquired. All the samples were measured by using a JEOL JEM-ARM300F at 300 kV. Elemental mapping and spectrum acquisition were obtained by using an Oxford Instruments INCA x-sight detector. Images were collected with a Gatan 1K × 1K CCD camera. The height and Young's modulus of nanosheet were tested by AFM (Dimension Icon, Bruker, USA) under the Peakforce QNM mode by using TAP150-G silicon cantilever. The acquired images with 512 × 512 pixels were analyzed using a NanoScope software version 14.12. The XRD patterns were recorded on a D8-Advance X-ray powder diffractometer (Bruker, USA) operated at voltage of 40 kV and current of 40 mA with CuK radiation (λ = 1.5406 Å).

2.3. Evaluation of photoelectrochemical activities

The acquired In_2S_3 nanosheets were initially dispersed in the solvent of ethanol to obtain a concentration of 1 mg/mL, and then 4.5 mL ethanol dispersion was uniformly spin-dropped on the 1.5 × 2 cm^2 ITO glass at 600 rpm by a desktop spin coater (KW-4A, made by the Chinese Academy of Sciences). The obtained electrode was heated at 100 °C for 180 min, thus the film was obtained for further measurements.

PEC tests were carried out in a conventional three-electrode, single compartment quartz cell filled with 0.1 M Na_2SO_4 electrolyte (pH = 7). The electrolyte was purged with nitrogen for 30 min before the measurement. The different morphologies of In_2S_3 (bulk, nanoparticles, nanosheets) deposited on ITO glass electrodes served as the working electrodes. The platinum wire was used as counter electrodes and Ag/AgCl was applied as a reference electrode. The PEC properties were measured on CHI 760E electrochemical analyzer (CHI Instrument, China) in ambient conditions under irradiation of a 300 W Xe lamp. The potential was swept from -0.6 to 0.8 V (versus Ag/AgCl) at a sweep rate of 0.05 V s^{-1}.

2.4. Photoelectrical water splitting

PEC tests were carried out in a conventional three-electrode, single compartment quartz cell filled with 0.5 M H_2SO_4 electrolyte (pH = 0) or 1 M KOH electrolyte (pH = 14). The electrolyte was purged with nitrogen for 30 min before the measurement. The Ru nanoparticle- and Co nanoparticle-doped In_2S_3 nanonsheets were deposited on ITO glass electrodes served as the working electrodes. For preparation of the electrode materials, catalyst powder was initially dispersed in the solvent of ethanol to obtain a concentration of 1 mg/mL, and then 4.5 mL ethanol dispersion was uniformly spin-dropped on the 1.5 × 2 cm^2 ITO glass at 600 rpm by a desktop spin coater (KW-4A, made by the Chinese Academy of Sciences). The platinum wire was used as counter electrodes. For HER, Ag/AgCl was used as a reference electrode. The potential was converted to potential versus RHE according to $E_{vs\ RHE} = E_{vs\ Ag/AgCl} + 0.0591 \times pH + 0.197$. For OER, Hg/HgO was used as reference electrode. The potential was converted to potential versus RHE according to $E_{vs\ RHE} = E_{vs\ Hg/HgO} + 0.0591 \times pH + 0.098$. The HER/OER catalytic activity was measured on CHI 760E electrochemical analyzer (CHI Instrument, China) in ambient conditions under irradiation of a 300W Xe lamp. The electrochemical tests were performed at room temperature.

2.5. Synchrotron X-ray absorption fine structure (XAFS) measurements

The indium L-edge XAFS was measured at the 4B7A beamline of Beijing Synchrotron Radiation Factory, Chinese Academy of Sciences (BSRF, CAS). Three modes (PFY, TEY and Transmission) are supplied for users to record XAFS spectrum in an energy region of 1750 eV–6000 eV.

2.6. Density functional theory (DFT) calculations

DFT as implemented in the form of Cambridge Sequential Total Energy Package (CASTEP) was used in calculation and geometric optimization for all the systems. Ultra-soft pseudopotential method was applied while the Generalized gradient approximation (GGA) in the scheme of PW91 was employed in the description of exchange-correlation interaction. The energy cutoff was set to 400 eV, and the convergence of energy was set to be 10^{-4} eV while that of force was 10^{-2} eV/Å. All of the models were calculated in periodically boxes with a vacuum slab of 15 Å to separate the interaction between periodic images. The size of the unit cell was 10.77 × 10.77 × 10.77 $Å^3$.

3. Results and discussions

3.1. Synthesis and characterization of ultrathin indium sulfide nanosheets

In_2S_3 ultrathin nanosheets were synthesized via thermal decomposition of indium acetate and sulfur precursors in a mixed solvent of octylamine and octane, an inert solvent with a molecular structure geometrically-matched to octylamine ligand. After heating to 250 °C for 12 h in an autoclave, purification of ultrathin nanosheets and removal of soft templates were achieved by washing five times with ethanol. Scanning transmission electron microscopy (STEM) revealed that free-standing, smooth and large-area sheet like nanostructure was acquired with a lateral dimension of ~1 μm, and the nearly transparent feature in transmission electron microscopy (TEM) revealed the ultrathin character of the nanosheet (Fig. 1a and b). The constituents of In and S were uniformly distributed throughout the nanosheets, as shown by energy dispersive spectroscopy (EDS) elemental mapping (Fig. S1). The acquired nanosheets were flexible with Young's modulus of 826 ± 153 MPa, and their thickness could be estimated through a folded layer exhibiting a fringe with a thickness of ~2.6 nm (Fig. 1c). Atomic force microscopy (AFM) further showed that the In_2S_3 nanosheets had a thickness of 2.59 ± 0.47 nm and lateral dimensions of 0.5–1.5 μm (Fig. 1f, Fig. S2). The crystal structure of the nanosheets was examined by X-ray diffraction (XRD), which revealed nearly identical lattice parameters to cubic In_2S_3 (lattice constants of a = b = c = 10.774 Å, JCPDS No. 65–0459) (Fig. 1g). High-angle annular dark-field scanning transmission electron microscopy (HAADF-STEM) demonstrated that the synthesized In_2S_3 nanosheets possessed a tetragonal phase with space group Fd-3m, and well-defined lattice fringes with interplanar distances of 0.31, 0.32 and 0.38 nm inferred to the {222}, {311} and {220} planes, respectively, of the cubic phase In_2S_3; these results corresponded well with the XRD results (Fig. 1d, cell model is shown in Supplementary material, Fig. S3). The selected area electron diffraction (SAED) pattern further revealed characteristic crystallographic orientations of highly crystalline In_2S_3 nanosheets with diffraction spots indexed to the $(2\bar{2}\bar{2})$, $(\bar{1}\bar{1}3)$, and $(0\bar{2}2)$ planes (Fig. 1e). The crystallographic data indicated that the ultrathin nanosheet surface was built by (422) crystal plane, and the thickness of nanosheet grew normal with respect to the [422] direction. The atomic model of ultrathin nanosheet was constructed with front and back sides composed of (422) planes (Fig. 1h and i), and the simulating single crystal diffraction pattern showed a similar intensity and metric distribution to that seen in the SAED pattern (Fig. 1e, Fig. S4). As the single-layer In_2S_3 slab along the [422] direction was ~0.88 nm, the vertical profile of nanosheet corresponded to three repeating units (Fig. S5).

3.2. Reaction mechanism of the geometrically matched alkane-assisted solution processing strategy

The anisotropic growth mechanism of the ultrathin nanosheets was further investigated by TEM in different reaction stages (Fig. 2). As shown in Fig. 2a, the success in synthesis of ultrathin nanosheets took advantage of an intermediate of In_2S_3 nucleus and a soft template formed via integrated assembly of amino ligands and an inert solvent. The process started with the formation of thioamide through the reaction of octylamine with sulfur [42,43]. The generated thioamide and accompanying by-product of hydrogen sulfide reacted with metal acetate to form a octahedron precursor (chemical formulas were shown in Supplementary material 1.5) [42], which subsequently merged into the nucleus at an energetically favorable site (Fig. 2b). The inert solvent,

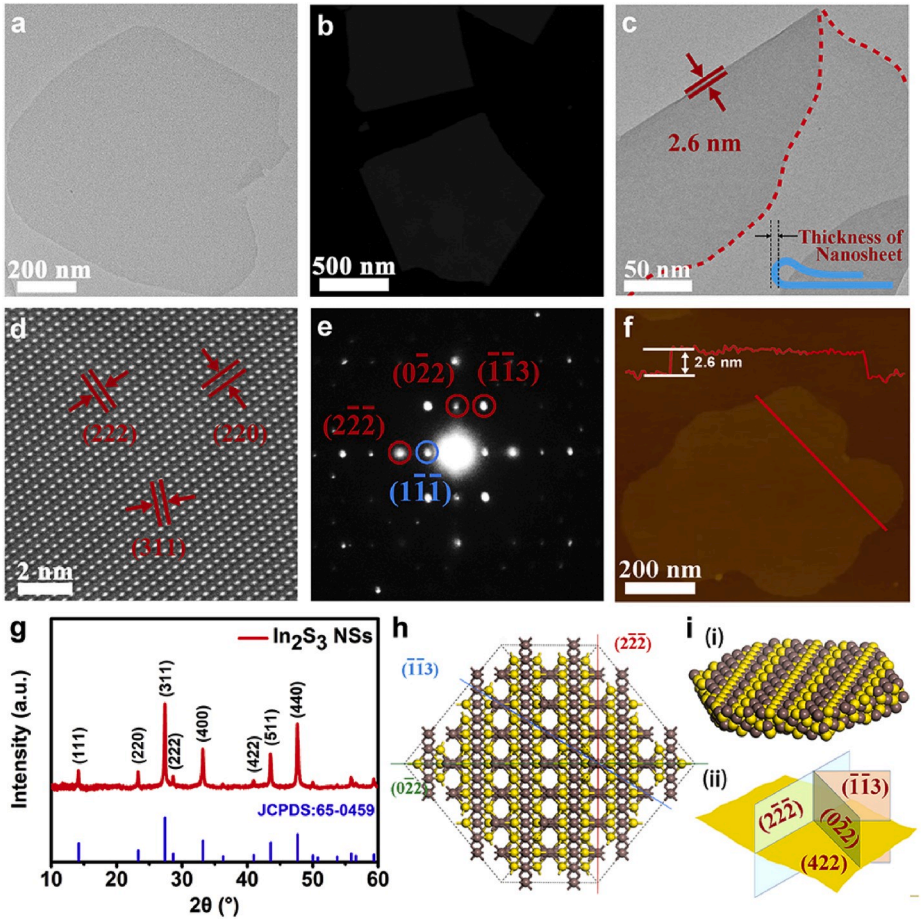

Fig. 1. Characterization of cubic-indium sulfide (In_2S_3) nanosheets. (a) Representative transmission electron microcopy (TEM) and (b) scanning transmission electron microscopy (STEM) images of In_2S_3 ultrathin nanosheets. (c) A representative TEM image of a folded single layer. (d) A representative high-angle annular dark-field scanning transmission electron microscopy (HAADF-STEM) image of In_2S_3 ultrathin nanosheets. (e) Corresponding selected area electron diffraction (SAED) pattern obtained with an aperture of ~0.7 μm in the middle of the nanosheet in (a). (f) Atomic force microscopy (AFM) scanning of In_2S_3 ultrathin nanosheets. The red line represents the height profile across the ultrathin nanosheet indicating a thickness of ~2.6 nm. (g) X-ray diffraction (XRD) pattern of nanosheets. Comparative data were from JCPDS card No. 65–0459. (h) Atomic structure of ultrathin nanosheet in vertical view from [422] direction. (i) Schematic diagram of ultrathin nanosheet from the oblique perspective.

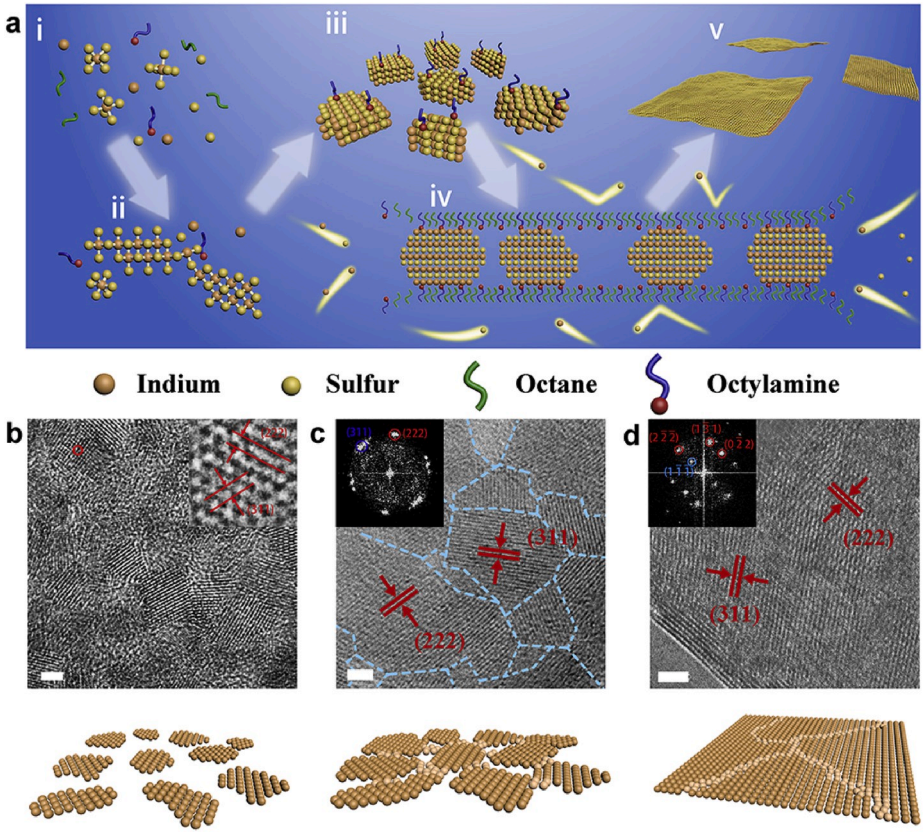

Fig. 2. Schematic diagram and TEM images demonstrating the growth mechanism of In_2S_3 nanosheets. (a) Schematic diagram of nanosheet formation process involving following steps: (i) thioamide reacted with indium acetate to form In–S octahedrons; (ii) aggregation of octahedrons; (iii) octahedrons merged into the nucleus at an energetically favorable site; (iv) 2D arrangement of the nucleus under the induction of soft template formed via integrated assembly of octylamine octane; (v) fusion of ultrathin nanosheets. (b–d) TEM images showing the time-dependent evolution of nanosheets. (b) Nuclei gathering together 5 min after the onset of the reaction. Scale bar = 10 nm. Inset: A high-resolution-transmission electron microcopy (HR-TEM) image of the area marked in (b). (c) More crystallized nuclei, about 5–6 nm in size, gathered together 30 min after the onset of the reaction. Scale bar = 2 nm. Inset: FFT pattern of (c). (d) A representative TEM image of the nearly fully formed nanosheet 6 h after the onset of the reaction. Scale bar = 2 nm. Inset: FFT pattern of (d). The three schematic drawings below each TEM image depict the structure of each time-dependent intermediate during the formation of the In_2S_3 nanosheets.

that is, octane played a crucial role in the templated growth of nanosheets. Once the nuclei had gathered together, the octane could self-assemble with capped ligands on the nucleus through inter-alkyl van der Waals forces, which may have precipitated the formation of a soft template that guided the lateral anisotropic arrangement of the nucleus (Fig. 2c) [44]. Based on the chemical inertness of the octane, the nucleus could hardly interact with the soft template, which facilitated the rotation of the nucleus and thus promoted the fusion of 2D nanosheets (Fig. 2d).

The surface energy of the crystal plane determines the anisotropic growth of the nanosheets. Facets with high surface energy show higher affinity for ligands, reducing the free energy of the system and improving the stability, while coverage of the ligand layer could block the delivery of reactants and the attachment of active precursors, resulting in thermodynamically controlled anisotropic growth [45]. To further understand the mechanism of anisotropic growth of ultrathin In_2S_3 nanosheets from a thermodynamic perspective, the formation energies of the facets shown in Fig. 1h and i as well as their binding energies to the ligand were further evaluated (Fig. S6, Tables S1 and S2). Density-functional theory (DFT) calculations indicated that the (422) plane of In_2S_3 possessed the highest formation energy, demonstrating high chemical activity in combination with ligands. The calculated ligand binding energy further confirmed that the surface free energy was significantly reduced once the ligand had coordinated with the (422) facet. These results provide intuitive evidence for understanding the reaction process: the amino ligands preferentially bond to the (422) plane of In_2S_3 seeds during the initial stage of the reaction, limiting the growth along the [422] direction. The solvent alkane molecules further self-assemble with the surface ligands to form a soft template, which induces the 2D arrangement of the nucleus, and finally fuses into the ultrathin nanosheets with the front and back sides exposing the (422) facets (Fig. 2a).

3.3. The chemical inertness and geometry of the alkane molecules regulates the morphology of nanostructures

As the main component of the soft template, the chemical inertness of alkane solvent molecules is an important prerequisite for achieving 2D fusion of seed crystals. The weak van der Waals forces between the octane molecules and seed crystals, where no covalent bonds are generated, avoids the limitation of crystal growth associated with template molecules. Moreover, the weak interaction between the template and In_2S_3 promotes rotation of the seed crystal, such that the optimal orientation can be self-adjusted to achieve anisotropic growth (Fig. 2c and d). To confirm the effect of the chemical inertness of the template on the crystal nanotopography, the reactions were carried out using a variety of templates with different octylamine and octane ratios. Fig. 3a showed that only nanoparticles, and not 2D nanosheets, formed when the template consisted entirely of amino ligands. This phenomenon is attributed to the high capacity for binding between the amino ligands and the In_2S_3 nucleus. Without chemically inert octane, octylamine could cap all exposed facets immediately (Fig. S7a), which inhibited growth in all directions resulting in a particle-like morphology. As the proportion of chemically inert octane increased, the nanotopography of the products gradually changed from particles to porous nanosheets (Fig. 3b and c). The reduction in the number of octylamine ligands led to exposure of the high-energy crystal planes of seed nuclei, in turn promoting lateral fusion of the intermediates (Figs. S7b and S7c). However, the strong interaction between the soft template and the seed crystals limited the adjustment, i.e., rotation and orientation of the nucleus, resulting in the formation of a porous nanostructure. Once the proportion of octane had increased to 98% of the total solvent volume, that is ~50 times the molar proportion of octylamine ligands, the holes of the nanosheets disappeared, and the unconstrained seeds fused into highly-crystalline nanosheets with integral surface structure (Fig. 3d, Fig. S7d).

Geometrical matching between amino ligands and alkane solvent

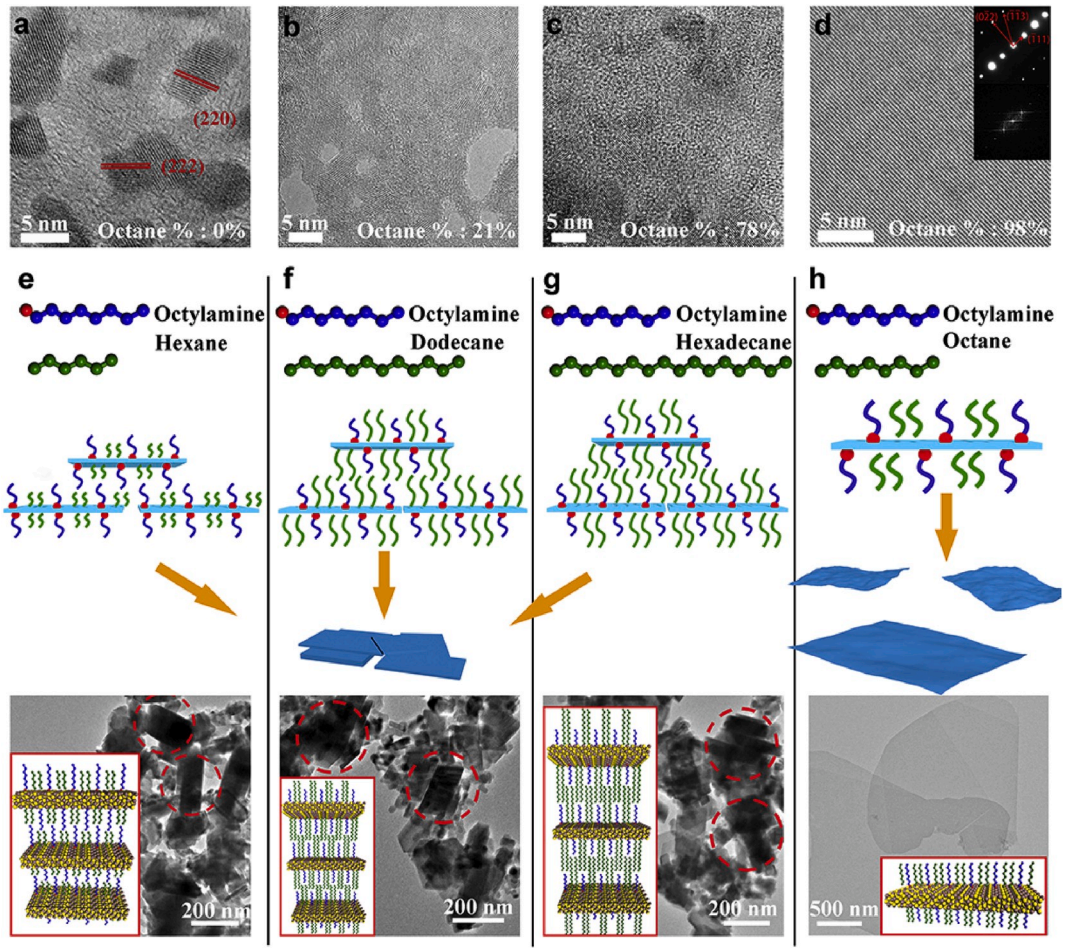

Fig. 3. TEM images and scheme diagrams illustrating the influence of inert solvents on the reaction products. (a–d) TEM images of products generated using different octylamine and octane ratios. (d). Inset: SAED pattern and FFT pattern of corresponding area in (d). (e–h) Scheme diagrams and TEM images of products using hexane (e), dodecane (f) hexadecane (g) and octane (h) as inert solvents.

molecules also lead to successful lateral self-assembly of the two components, in turn giving rise to the formation of a 2D soft template. In contrast, a molecular configuration mismatch between the ligand and the alkane solvent will introduce vacancies and defects on the surface of the template, which promotes docking between adjacent templates, similar to Lego blocks packed in a staggered formation; this gives rise to nanosheet aggregation in the longitudinal direction (Fig. S8). To confirm this, geometry mismatch models were established by replacing octane (C_8) with hexane (C_6), dodecane (C_{12}) or hexadecane (C_{16}), respectively (Fig. 3e, f, 3g). The TEM results demonstrated that the mismatch between the alkane and amino ligand geometry facilitated the accumulation and interlocking of small nanosheets to yield thick nano-chunks (Fig. 3e, f, 3g). In contrast, the well-matched geometry of octylamine and octane avoided surface vacancy-induced template docking, such that thickness control of the nanosheets was achieved (Fig. 3h).

3.4. The geometrically-matched alkane-assisted solution processing strategy is general

Interestingly, our geometrically-matched alkane-assisted solution processing strategy is not limited to fabrication of In_2S_3 nanosheets; it can be extended to the synthesis of a variety of 2D metal chalcogenides. To further evaluate the generality of this strategy, we synthesized five other kinds of 2D nanostructures, i.e., Co_9S_8, MnS, SnS_2, Al_2S_3 and MoS_2, and nanosheets, by simply altering the chemical composition and stoichiometry of the metal precursor (Fig. 4, Figs. S9 and S10). For example, MnS nanosheets were obtained by thermal decomposition of equivalent doses of manganese (II) chloride tetrahydrate and sulfur powder in a mixed solvent of octylamine and octane (octylamine/octane = 2%/98%) (**Details in Supplementary material 1.2**). This approach has several advantages, such as simple operation, low cost, and the simple removal of the soft template due to the chemical inertness of the alkane without any chemical adsorption by nanocrystals. Therefore, the developed strategy has potential for large-scale fabrication of a broad portfolio 2D nanomaterials.

3.5. Synchrotron X-ray absorption fine structure measurements

To quantitatively evaluate the atomic parameters of In_2S_3 ultrathin nanosheets, synchrotron radiation X-ray absorption fine structure spectra (XAFS) measurements at In L_3-edge were performed at the Beijing Synchrotron Radiation Facility, Chinese Academy of Sciences, China [46]. The In L_3-edge $k^3\chi(k)$ oscillation curve for In_2S_3 ultrathin nanosheets displayed remarkable differences compared with bulk In_2S_3 and In_2S_3 nanoparticles (~8 nm in diameter, **Supplementary material 1.4**), especially in the 2–6 $Å^{-1}$ k-region, suggesting differences in atomic arrangement among the three In_2S_3 morphologies (Fig. 5a, Fig. S11). The differences were shown more clearly by the corresponding Fourier transforms in k-space, as illustrated in Fig. 5b. The two main peaks, at 2.36 and 3.74 Å, corresponded to the nearest In–S and next-nearest In–In coordination, respectively, and characterized the R-space curve of bulk In_2S_3 [47]. For the In_2S_3 nanoparticles, the intensities of the two peaks were decreased along with a slight shift to the higher -R side. Moreover, a new peak centered at 1.33 Å appeared, verifying the presence of

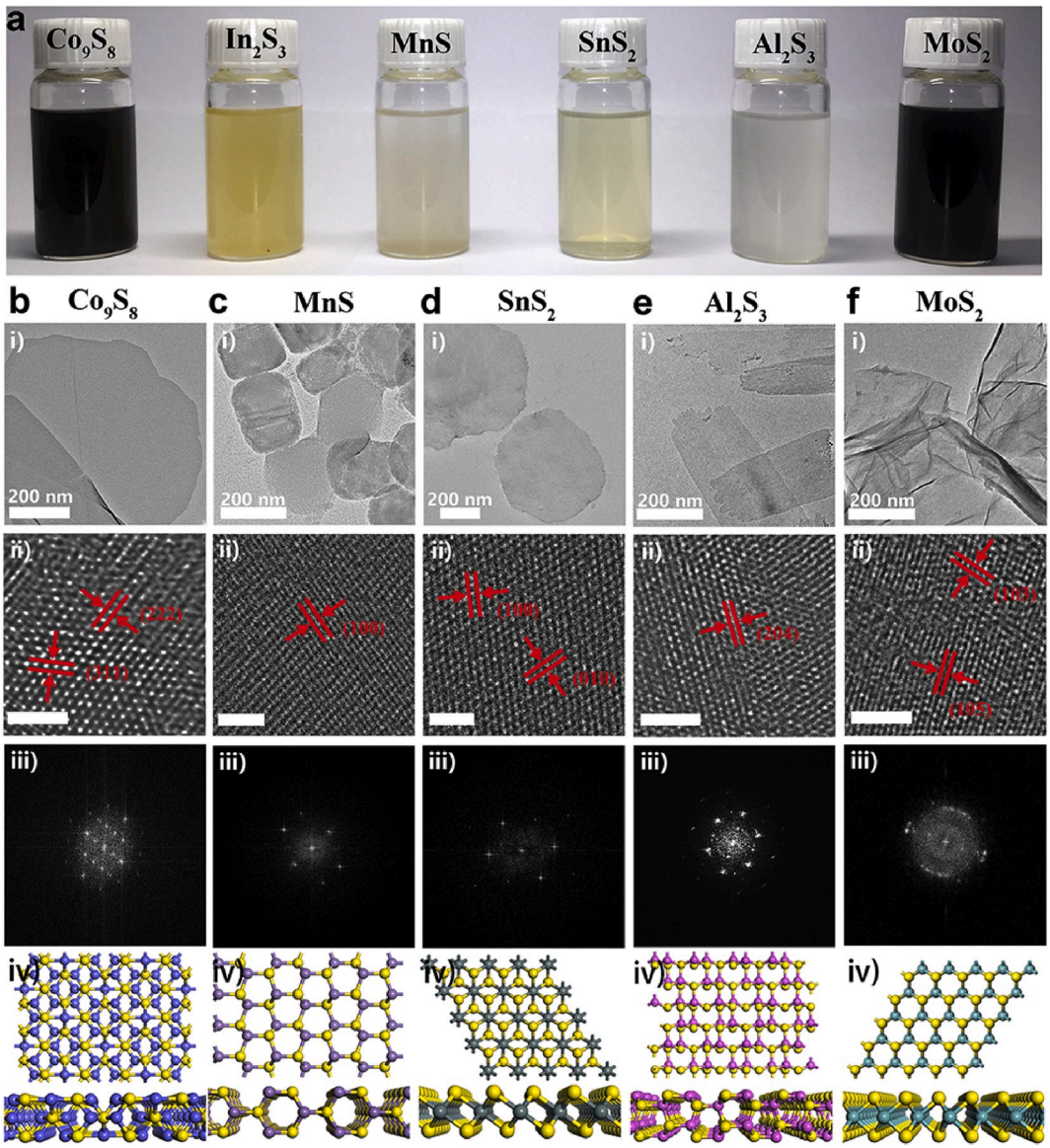

Fig. 4. Characterization and schematic models of synthesized two-dimensional (2D) metal sulfide. (a) Optical photographs of as-prepared 2D nanosheets. (b–f) Characterization and schematic models of Co_9S_8 (b), MnS (c), SnS_2 (d), Al_2S_3 (e) and MoS_2 (f). (i) TEM images of ethanol diffusion of the metal sulfide. (ii) HR-TEM images of area marked in (i). Scale bar = 2 nm. (iii) FFT pattern of area marked in (ii). (iv) Schematic models of 2D metal sulfide.

capped ligands [48]. In contrast, the *r*-space curve for the ultrathin nanosheets indicated that the In–S peak was further shifted to 2.43 Å associated with obviously decreased In–S and In–In peak intensities. Interestingly, unlike nanoparticles, the peak at 1.33 Å was hardly observed in the nanosheet group, confirming only small amounts of ligand residues covered on the surface of the nanocrystals with use of our synthetic strategy. The significant reduction of peak intensities, and the shift of peak positions to the higher *-R* side of the ultrathin nanosheets, demonstrated the distortion of the surface atomic structure, which could trigger different photoelectric responses [48]. The density of states (DOS) values for In_2S_3 ultrathin nanosheets and their bulk counterparts are shown in Fig. 5c. Compared with the DOS of bulk In_2S_3, the In_2S_3 ultrathin nanosheets exhibited an increased density at the edge of the conduction band and the valence band, which could be due to structural distortions of the ultrathin topology. It has been proven that the optical absorption, separation and immigration capacities of photogenerated charge carriers are positively correlated with the DOS [20,49,50]. Therefore, ultrathin nanosheets with a large DOS will inevitably possess a high carrier migration rate, thus ensuring their high photoelectric activity.

3.6. Photoelectrical properties and photoelectrochemical applications

The ultrathin nanosheets could shorten the carrier diffusion length along the *c*-axis, thus overcoming the recombination of electron-hole pairs and facilitating the photogenerated carriers with respect to reaching the catalytically active center on the surface and thus participating in chemical reactions. Compared with the In_2S_3 nanoparticles, ultrathin In_2S_3 nanosheets exhibited distinct optical and photoelectric responses. In the nanosheet group, blueshifts occurred in emission peak, accompanied by a significant reduction in photoluminescence (PL) intensity (Fig. S12), which in turn contributed to the strong quantum confinement effect and enhanced carrier mobility of ultrathin nature. The photoelectronic properties were further assessed with reference to the surface photovoltaic (SPV) spectrum from the ultraviolet to the visible region (Fig. 5d). The ultrathin In_2S_3 nanosheets exhibited remarkable enhancement in the SPV response, approximately 5- and 41-fold higher than that of nanoparticles and their bulk counterparts, thus

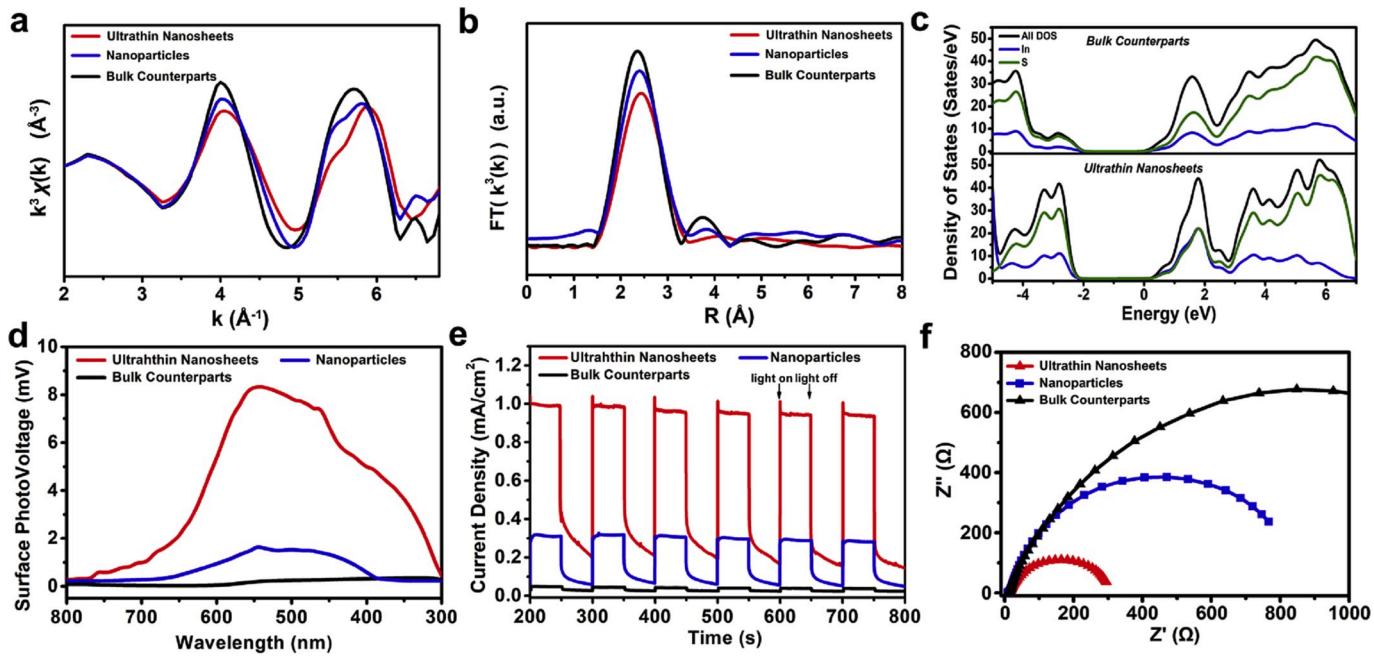

Fig. 5. Synchrotron radiation X-ray absorption fine structure spectra (XAFS) measurements, calculated density of states (DOS) values and photoelectrochemical (PEC) properties. (a) Indium L_3-edge $k^3\chi$ (k) oscillation curve for the In_2S_3 ultrathin nanosheets, In_2S_3 nanoparticles and bulk In_2S_3. (b) Corresponding Fourier transforms in k-space of (a). (c) The calculated DOS of total, sulfur and indium state density of In_2S_3 ultrathin nanosheets and bulk In_2S_3. (d) Surface photovoltage spectroscopy of In_2S_3 ultrathin nanosheets, In_2S_3 nanoparticles and bulk In_2S_3. (e) I-t curves of In_2S_3 ultrathin nanosheets, In_2S_3 nanoparticles and bulk In_2S_3.at 0.8 V versus Ag/AgCl with/without irradiation of 300 W Xe lamp. (f) Electrochemical impedance spectra of In_2S_3 ultrathin nanosheets, In_2S_3 nanoparticles and bulk In_2S_3. at 0.8 V versus Ag/AgCl under 300 W Xe lamp irradiation (Z′ and Z″ are the real and imaginary parts of the impedance).

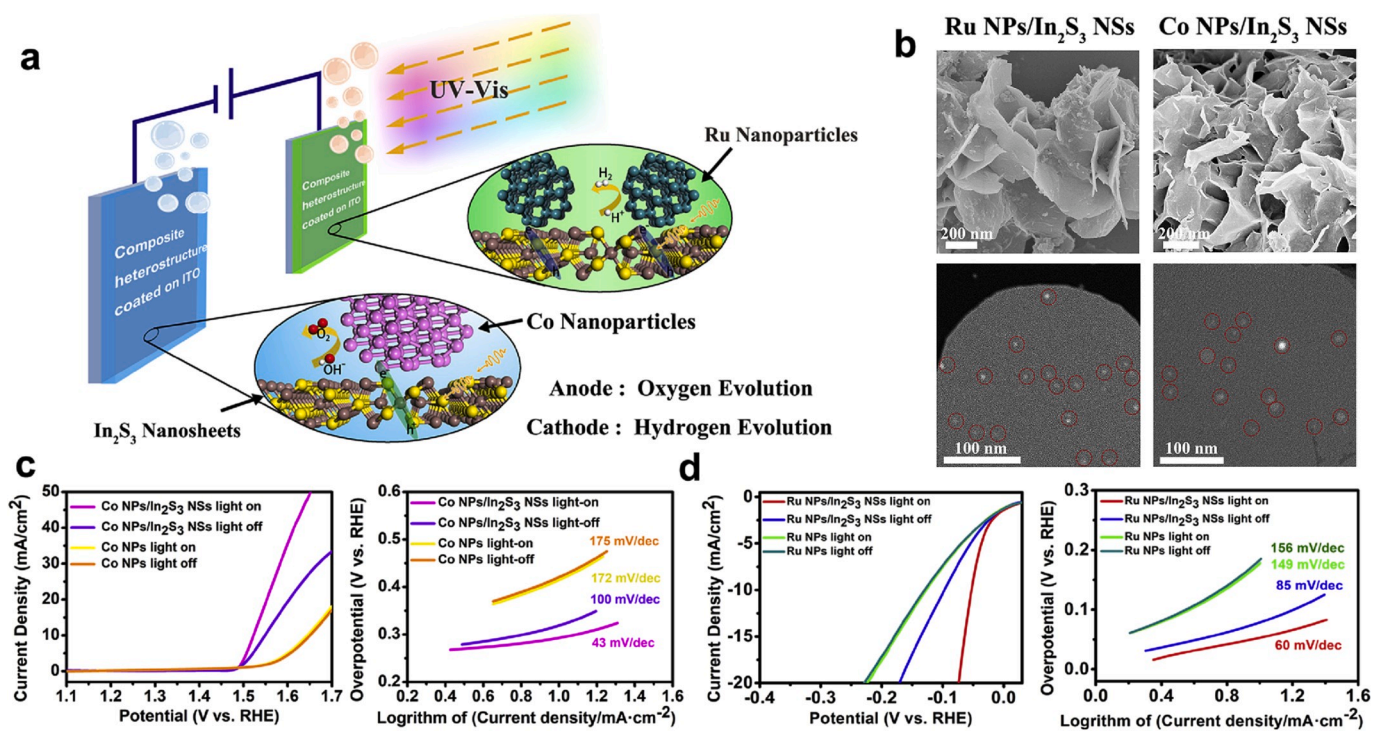

Fig. 6. Morphology of Ru/Co nanoparticle-doped In_2S_3 ultrathin nanosheets and their PEC water splitting performance. (a) Schematic diagram of a PEC solar water splitting device. (b) Scanning electron microscopy (SEM) and STEM of Ru nanoparticles-doped In_2S_3 nanosheets (left), and Co nanoparticles-doped In_2S_3 nanosheets (right) (c) Light-on and -off linear sweep voltammetry curves (left) and their corresponding Tafel plots (right) of Co nanoparticles-doped In_2S_3 nanosheets and Co nanoparticles coated on ITO substrate in 1 M KOH electrolyte. (d) Light-on and -off linear sweep voltammetry curves (left) and their corresponding Tafel plots (right) of Ru nanoparticles-doped In_2S_3 nanosheets and Ru nanoparticles coated on ITO substrate in 0.5 M H_2SO_4 electrolyte. 300 W Xe lamp was used in the light-on condition.

illustrating efficient separation and transportation of photogenerated carriers. The PEC properties of ultrathin In_2S_3 nanosheets were recorded via a three-electrode setup in 0.1 M Na_2SO_4 electrolyte. As shown in Fig. S13a, the nanosheets displayed a much-enhanced photocurrent density of 1.02 mA cm^{-2} at 0.8 V under illumination of Xe lamps (0.20 mA cm^{-2} in the dark field), nearly 3.2 and 20.4 times larger than that of In_2S_3 nanoparticles (0.32 mA cm^{-2}) and their bulk counterpart (0.05 mA cm^{-2}), respectively, under the same illumination conditions (Fig. S13b). The photocurrent densities of nanosheets showed negligible variation even after 300min of irradiation (Fig. S13c), demonstrating their excellent photostability. Moreover, the ultrathin crystalline nanosheets, with high photoresponsivity, showed efficient on/off photoswitching properties, and their photocurrent density remained stable after several cycles, being roughly 25 times higher than that of the bulk counterpart (Fig. 5e). The electrochemical impedance spectra further illustrated that the nanosheets exhibited a much smaller electrical resistance (110 Ω) than the nanoparticles (386 Ω) and their bulk counterpart (676 Ω) (Fig. 5f), which suggested that the ultrathin 2D features could achieve a better boundary connectivity and intimate contact with the indium tin oxide (ITO) substrate, resulting in efficient photoelectron transfer kinetics at the interface of the In_2S_3 nanosheet and the electrolyte.

The morphological advantages of our approach led to superior photoelectric activities, making the ultrathin In_2S_3 nanosheet an excellent candidate for fabrication efficient photoelectrode for PEC water splitting [51,52]. To boost the reaction, heterogeneous structures composed of semiconductors and catalytically active metal components were developed, in which the charge carriers were separated by absorbed light and further migrated to the photoelectrode/electrolyte junction to generate oxygen/hydrogen. Therefore, the ultrathin In_2S_3 nanosheets were loaded with Ru and Co nanoparticles (separately) for efficient hydrogen evolution reactions (HER) and oxygen evolution reactions (OER), respectively (Fig. 6a and b, Figs. S14 and S15). In the dark field, heterogeneous photoelectrocatalysts exhibited lower overpotentials than the monocomponent metal electrocatalysts (Ru or Co nanoparticles), yet still higher than that of in the bright field in terms of both the HER and OER, due to the strongly localized ground state of the semiconductor nanosheets [53]. However, the hybrid photoelectrodes exhibited significantly enhanced catalytic activities toward HER and OER under the illumination condition. As observed, the excited Ru nanoparticle-doped In_2S_3 nanosheets exhibited a much smaller overpotential of 53.6 mV than their ground states (97.9 mV) at a current density of 10 mA cm^{-2} in HER; the same trend was observed in OER (overpotential of 293.6 mV under light excitation vs. that of 319.8 mV in the dark field at a current density of 10 mA cm^{-2}). In contrast, light irradiation showed little effect on the catalytic performances of monocomponent metal electrocatalysts (~130 mV of Ru nanoparticles in HER, ~421 mV of Co nanoparticle in OER) (Fig. 6c and d). The single-component catalytic activities of In_2S_3 nanosheets were also tested. Although the catalytic performance of nanosheets could be improved under the illumination condition, the HER and OER activities of single-component In_2S_3 nanosheets were incomparable with that of heterogeneous catalysts (Fig. S16). The Tafel slope of Ru nanoparticle- and Co nanoparticle-doped In_2S_3 nanonsheets under illumination was 60 mV $decade^{-1}$ (HER) and 43 mV $decade^{-1}$ (OER), respectively, which was always smaller than that of Ru and Co nanoparticles (Fig. 6c and d). To further confirm the effect of the 2D nanostructure of In_2S_3 on the catalytic performance of heterogeneous photoelectrocatalysts, other heterostructures were constructed by doping Ru/Co nanoparticle on different In_2S_3 morphologies. The results showed that both bulk In_2S_3- and In_2S_3 nanoparticles-based heterogeneous catalysts exhibited much higher overpotentials and Tafel slopes than that of In_2S_3 nanosheet-based catalysts (Fig. S17). The underlying mechanism should be attributed to the unique surface effect of ultrathin In_2S_3 nanosheet. The nanosheets, possessing large surface area, can effectively increase the absorption of photons, resulting in higher light harvest efficiency under the same irradiation conditions [54,55]. Moreover, The ultrathin 2D structure could bring new surface states, more exposed active sites, and shorter diffusion paths of photogenerated charge carriers to the material, which result in efficient separation and transportation of carriers, thereby improving the photoelectrocatalytic activities [20]. The results confirmed that the ultrathin In_2S_3 nanosheets could provide a versatile platform for a variety of PEC applications.

4. Conclusion

In summary, we synthesized ultrathin nanosheets by developing a geometrically-matched alkane-assisted solution processing strategy, in which amino ligands and inert solvent were integrated to form a 2D template, guiding the anisotropic growth of nanosheets. The ligand and inert solvent synergistically regulated nanostructures, through matching their molecular configurations and optimizing the stoichiometry. The approach developed herein could be extended to synthesis of various 2D metal chalcogenides. The prepared ultrathin In_2S_3 nanosheets, possessing high photoelectric activities, could be utilized to fabricate composite photoelectrodes after the loading of metal nanoparticles to achieve efficient PEC water splitting. Our work provides new perspectives for the synthesis of 2D materials for further applications to catalysis, electronic devices and energy harvesting.

Declaration of competing interest

The authors declare no conflict of interest.

CRediT authorship contribution statement

Dan Luo: Conceptualization, Project administration, Writing - original draft. **Boyang Zhou:** Investigation, Methodology, Writing - original draft. **Bowen Guo:** Data curation, Formal analysis. **Peng Gao:** Formal analysis. **Lei Zheng:** Formal analysis. **Xiaojun Zhang:** Formal analysis. **Shengjie Cui:** Formal analysis. **Hongjun Zhou:** Funding acquisition. **Yongsheng Zhou:** Writing - review & editing. **Yan Liu:** Writing - review & editing.

Acknowledgements

D. L. and B. Z. contributed equally to this paper. The authors declare no conflict of interests in this work. We would like to thank Beijing Synchrotron Radiation Facility technical support groups. This work was supported by the National Natural Science Foundations of China No. 51902344 (D. L.), No. 81871492 (Y. L.) and No. 81571815 (Y. L.), the Beijing Municipal Natural Science Foundation No. 2184119 (D. L.), Projects of Beijing Nova Programme Interdisciplinary Cooperation No. Z181100006218135 (Y. L. and D. L.), Beijing New-star Plan of Science and Technology No. Z171100001117018 (Y. L.), the Science Foundation of China University of Petroleum No. 2462018BJB002 (D. L.) and Project for Culturing Leading Talents in Scientific and Technological Innovation of Beijing No. Z171100001117169 (Y.Z.).

Appendix A. Supplementary data

Supplementary data to this article can be found online at https://doi.org/10.1016/j.nanoen.2020.104689.

References

[1] H. Wang, H. Yuan, S.S. Hong, Y. Li, Y. Cui, Physical and chemical tuning of two-dimensional transition metal dichalcogenides, Chem. Soc. Rev. 44 (2015) 2664–2680.
[2] S. Manzeli, D. Ovchinnikov, D. Pasquier, O.V. Yazyev, A. Kis, 2D transition metal dichalcogenides, Nat. Rev. Mater. 2 (2017) 17033.
[3] H. Zhang, H.M. Cheng, P. Ye, 2D nanomaterials: beyond graphene and transition metal dichalcogenides, Chem. Soc. Rev. 47 (2018) 6009–6601.

[4] A.J. Mannix, B. Kiraly, M.C. Hersam, N.P. Guisinger, Synthesis and chemistry of elemental 2D materials, Nat. Rev. Chem. 1 (2017), 0014.
[5] Z. Sun, A. Martinez, F. Wang, Optical modulators with 2D layered materials, Nat. Photon. 10 (2016) 227.
[6] J.R. Schaibley, H. Yu, G. Clark, P. Rivera, J.S. Ross, K.L. Seyler, W. Yao, X. Xu, Valleytronics in 2D materials, Nat. Rev. Mater. 1 (2016) 16055.
[7] D.A. Bandurin, A.V. Tyurnina, L.Y. Geliang, A. Mishchenko, V. Zólyomi, S. V. Morozov, R.K. Kumar, R.V. Gorbachev, Z.R. Kudrynskyi, S. Pezzini, Z. D. Kovalyuk, U. Zeitler, K.S. Novoselov, A. Patane, L. Eaves, I.V. Grigorieva, V. I. Fal'ko, A.K. Geim, Y. Cao, High electron mobility, quantum Hall effect and anomalous optical response in atomically thin InSe, Nat. Nanotechnol. 12 (2017) 223.
[8] Y. Ma, L. Kou, X. Li, Y. Dai, S.C. Smith, T. Heine, Quantum spin Hall effect and topological phase transition in two-dimensional square transition-metal dichalcogenides, Phys. Rev. B 92 (2015), 085427.
[9] Z. Liu, G. Zhao, B. Liu, Z.F. Wang, J. Yang, F. Liu, Intrinsic quantum anomalous hall effect with in-plane magnetization: searching rule and material prediction, Phys. Rev. Lett. 121 (2018) 246401.
[10] P. Rivera, K.L. Seyler, H. Yu, J.R. Schaibley, J. Yan, D.G. Mandrus, W. Yao, X. Xu, Valley-polarized exciton dynamics in a 2D semiconductor heterostructure, Science 351 (2016) 688–691.
[11] C. Xu, L. Wang, Z. Liu, L. Chen, J. Guo, N. Kang, X. Ma, H. Cheng, W. Ren, Large-area high-quality 2D ultrathin Mo 2 C superconducting crystals, Nat. Mater. 14 (2015) 1135.
[12] A.W. Tsen, B. Hunt, Y.D. Kim, Z.J. Yuan, S. Jia, R.J. Cava, J. Hone, P. Kim, C. R. Dean, A.N. Pasupathy, Nature of the quantum metal in a two-dimensional crystalline superconductor, Nat. Phys. 12 (2016) 208.
[13] S.J. Kim, K. Choi, B. Lee, Y. Kim, B.H. Hong, Materials for flexible, stretchable electronics: graphene and 2D materials, Annu. Rev. Mater. Res. 45 (2015) 63–84.
[14] Z. Pan, B. Liu, J. Zhai, L. Yao, K. Yang, B. Shen, $NaNbO_3$ two-dimensional platelets induced highly energy storage density in trilayered architecture composites, Nano Energy 40 (2017) 587–595.
[15] Q.H. Wang, K. Kalantar-Zadeh, A. Kis, J.N. Coleman, M.S. Strano, Electronics and optoelectronics of two-dimensional transition metal dichalcogenides, Nat. Nanotechnol. 7 (2012) 699.
[16] F. Ming, H. Liang, Y. Lei, W. Zhang, H.N. Alshareef, Solution synthesis of VSe_2 nanosheets and their alkali metal ion storage performance, Nano Energy 53 (2018) 11–16.
[17] G. Fiori, F. Bonaccorso, G. Iannaccone, T. Palacios, D. Neumaier, A. Seabaugh, S. K. Banerjee, L. Colombo, Electronics based on two-dimensional materials, Nat. Nanotechnol. 9 (2014) 768.
[18] H. Li, Y. Shi, M.H. Chiu, L.J. Li, Emerging energy applications of two-dimensional layered transition metal dichalcogenides, Nano Energy 18 (2015) 293–305.
[19] J. Xu, J. Mahmood, Y. Dou, S. Dou, F. Li, L. Dai, J.B. Baek, 2D frameworks of C_2N and C_3N as new anode materials for lithium-ion batteries, Adv. Mater. 29 (2017) 1702007.
[20] D. Deng, K.S. Novoselov, Q. Fu, N. Zheng, Z. Tian, X. Bao, Catalysis with two-dimensional materials and their heterostructures, Nat. Nanotechnol. 11 (2016) 218.
[21] Q. Fu, X. Bao, Surface chemistry and catalysis confined under two-dimensional materials, Chem. Soc. Rev. 46 (2017) 1842–1874.
[22] Q. Liang, L. Zhong, C. Du, Y. Luo, Y. Zheng, S. Li, Q. Yan, Achieving highly efficient electrocatalytic oxygen evolution with ultrathin 2D Fe-doped nickel thiophosphate nanosheets, Nano Energy 47 (2018) 257–265.
[23] W. Zhang, Y. Hu, L. Ma, G. Zhu, P. Zhao, X. Xue, R. Chen, S. Yang, J. Ma, J. Liu, Z. Jin, Liquid-phase exfoliated ultrathin Bi nanosheets: uncovering the origins of enhanced electrocatalytic CO_2 reduction on two-dimensional metal nanostructure, Nano Energy 53 (2018) 808–816.
[24] Z. Xiang, Y. Xue, D. Cao, L. Huang, J.F. Chen, L. Dai, Highly efficient electrocatalysts for oxygen reduction based on 2D covalent organic polymers complexed with non-precious metals, Angew. Chem. Int. Ed. 53 (2014) 2433–2437.
[25] X. Wang, G. Sun, N. Li, P. Chen, Quantum dots derived from two-dimensional materials and their applications for catalysis and energy, Chem. Soc. Rev. 45 (2016) 2239–2262.
[26] Y. Zhu, L. Peng, Z. Fang, C. Yan, X. Zhang, G. Yu, Structural engineering of 2D nanomaterials for energy storage and catalysis, Adv. Mater. 30 (2018) 1706347.
[27] J. Di, J. Xia, H. Li, Z. Liu, Freestanding atomically-thin two-dimensional materials beyond graphene meeting photocatalysis: opportunities and challenges, Nano Energy 35 (2017) 79–91.
[28] Z. Xiang, D. Cao, L. Huang, J. Shui, M. Wang, L. Dai, Nitrogen-doped holey graphitic carbon from 2D covalent organic polymers for oxygen reduction, Adv. Mater. 26 (2014) 3315–3320.
[29] P. Zhao, Y. Ma, X. Lv, M. Li, B. Huang, Y. Dai, Two-dimensional III2-VI3 materials: promising photocatalysts for overall water splitting under infrared light spectrum, Nano Energy 51 (2018) 533–538.
[30] H. Yin, Z. Tang, Ultrathin two-dimensional layered metal hydroxides: an emerging platform for advanced catalysis, energy conversion and storage, Chem. Soc. Rev. 45 (2016) 4873–4891.
[31] R.S. Datta, J.Z. Ou, M.D. Mohiuddin, B.J. Carey, B.Y. Zhang, H. Khan, N. Syed, A. Zavabeti, F. Haque, T. Daeneke, K. Kalantar-zadeh, Two dimensional PbMoO4: a photocatalytic material derived from a naturally non-layered crystal, Nano Energy 49 (2018) 237–246.
[32] X. Xiao, C.T. He, S. Zhao, J. Li, W. Lin, Z. Yuan, Q. Zhang, S.Y. Wang, L.M. Dai, D. Yu, A general approach to cobalt-based homobimetallic phosphide ultrathin nanosheets for highly efficient oxygen evolution in alkaline media, Energy Environ. Sci. 10 (2017) 893–899.
[33] Z. Yuan, J. Li, M. Yang, Z. Fang, J. Jian, D. Yu, X. Chen, L. Dai, Ultrathin black phosphorus-on-nitrogen doped graphene for efficient overall water splitting: dual modulation roles of directional interfacial charge transfer, J. Am. Chem. Soc. 141 (2019) 4972–4979.
[34] Y. Shi, W. Zhou, A.Y. Lu, W. Fang, Y.H. Lee, A.L. Hsu, S.M. Kim, K.K. Kim, H. Y. Yang, L.J. Li, J.C. Idrobo, J. Kong, van der Waals epitaxy of MoS_2 layers using graphene as growth templates, Nano Lett. 12 (2012) 2784–2791.
[35] L. Liu, J. Park, D.A. Siegel, K.F. McCarty, K.W. Clark, W. Deng, L. Basile, J. C. Idrobo, G. Gu, Heteroepitaxial growth of two-dimensional hexagonal boron nitride templated by graphene edges, Science 343 (2014) 163–167.
[36] J.N. Coleman, M. Lotya, A. O'Neill, S.D. Bergin, P.J. King, U. Khan, K. Young, A. Gaucher, S. De, R.J. Smith, I.V. Shvets, S.K. Arora, G. Stanton, H.Y. Kim, K. Lee, G.T. Kim, G.S. Duesberg, T. Hallam, J.J. Boland, J.J. Wang, J.F. Donegan, J. C. Grunlan, G. Moriarty, A. Shmeliov, R.J. Nicholls, J.M. Perkins, E.M. Grieveson, K. Theuwissen, D.W. McComb, P.D. Nellist, V. Nicolosi, Two-dimensional nanosheets produced by liquid exfoliation of layered materials, Science 331 (2011) 568–571.
[37] V. Nicolosi, M. Chhowalla, M.G. Kanatzidis, M.S. Strano, J.N. Coleman, Liquid exfoliation of layered materials, Science 340 (2013) 1226419.
[38] W. Zhu, T. Low, Y.H. Lee, H. Wang, D.B. Farmer, J. Kong, F. Xia, P. Avouris, Electronic transport and device prospects of monolayer molybdenum disulphide grown by chemical vapour deposition, Nat. Commun. 5 (2014) 3087.
[39] Y. Shi, H. Li, L.J. Li, Recent advances in controlled synthesis of two-dimensional transition metal dichalcogenides via vapour deposition techniques, Chem. Soc. Rev. 44 (2015) 2744–2756.
[40] Q. Ji, Y. Zhang, Y. Zhang, Z. Liu, Chemical vapour deposition of group-VIB metal dichalcogenide monolayers: engineered substrates from amorphous to single crystalline, Chem. Soc. Rev. 44 (2015) 2587–2602.
[41] J. Zhou, J. Lin, X. Huang, Y. Zhou, Y. Chen, J. Xia, H. Wang, Y. Xie, H. Yu, J. Lei, D. Wu, F. Liu, Q. Fu, Q. Zeng, C. Huang, C. Yang, L. Lu, T. Yu, Z. Shen, H. Lin, B. I. Yakobson, Q. Liu, K. Suenaga, G. Liu, Z. Liu, A library of atomically thin metal chalcogenides, Nature 556 (2018) 355.
[42] J.W. Thomson, K. Nagashima, P.M. Macdonald, G.A. Ozin, From sulfur− amine solutions to metal sulfide nanocrystals: peering into the oleylamine− sulfur black box, J. Am. Chem. Soc. 133 (2011) 5036–5041.
[43] S. Mourdikoudis, L.M. Liz-Marzan, Oleylamine in nanoparticle synthesis, Chem. Mater. 25 (2013) 1465–1476.
[44] C. Schliehe, B.H. Juarez, M. Pelletier, S. Jander, D. Greshnykh, M. Nagel, A. Meyer, S. Foerster, A. Kornowski, C. Kinke, H. Weller, Ultrathin PbS sheets by two-dimensional oriented attachment, Science 329 (2010) 550–553.
[45] M.A. Boles, D. Ling, T. Hyeon, D.V. Talapin, The surface science of nanocrystals, Nat. Mater. 15 (2016) 141–153.
[46] Y. Sun, S. Gao, F. Lei, C. Xiao, Y. Xie, Ultrathin two-dimensional inorganic materials: new opportunities for solid state nanochemistry, Acc. Chem. Res. 48 (2014) 3–12.
[47] M. Epple, M. Panthöfer, R. Walther, H.J. Deiseroth, Crystal-chemical characterization of mixed-valent indium chalcogenides by X-ray absorption spectroscopy (EXAFS), Z. Krist. Cryst. Mater. 215 (2000) 445–453.
[48] Y. Sun, Z. Sun, S. Gao, H. Cheng, Q. Liu, J. Piao, T. Yao, C. Wu, S. Hu, S. Wei, Y. Xie, Fabrication of flexible and freestanding zinc chalcogenide single layers, Nat. Commun. 3 (2012) 1057.
[49] M. Madl, W. Brezna, P. Klang, A.M. Andrews, G. Strasser, J. Smoliner, High resolution photocurrent imaging by atomic force microscopy on the example of single buried InAs quantum dots, Semicond. Sci. Technol. 25 (2010), 065010.
[50] Y. Sun, H. Cheng, S. Gao, Z. Sun, Q. Liu, Q. Liu, F. Lei, T. Yao, J. He, S. Wei, Y. Xie, Freestanding tin disulfide singl-layers realizing efficient visible-light water splitting, Angew. Chem. Int. Ed. 51 (2012) 8727–8731.
[51] T. Hisatomi, J. Kubota, K. Domen, Recent advances in semiconductors for photocatalytic and photoelectrochemical water splitting, Chem. Soc. Rev. 43 (2014) 7520–7535.
[52] S. Gao, Y. Sun, F. Lei, J. Liu, L. Liang, T. Li, B. Pan, J. Zhou, Y. Xie, Freestanding atomically-thin cuprous oxide sheets for improved visible-light photoelectrochemical water splitting, Nano Energy 8 (2014) 205–213.
[53] A. Shabaev, A.L. Efros, A.L. Efros, Dark and photo-conductivity in ordered array of nanocrystals, Nano Lett. 13 (2013) 5454–5461.
[54] M. Faraji, M. Yousefi, S. Yousefzadeh, M. Zirak, N. Naseri, T. Jeon, W. Choi, A. Moshfegh, Two-dimensional materials in semiconductor photoelectrocatalytic systems for water splitting, Energy Environ. Sci. 12 (2019) 59–95.
[55] Z. Yin, B. Chen, M. Bosman, X. Cao, J. Chen, B. Zheng, H. Zhang, Au nanoparticle-modified MoS_2 nanosheet-based photoelectrochemical cells for water splitting, Small 10 (2014) 3537–3543.

Dan Luo is an associate professor at College of New Energy and Materials, China University of Petroleum-Beijing. He received his BSc (2008) and PhD (2013) degrees at Peking University Health Science Center. Before he joined in China University of Petroleum-Beijing (2015), he worked as an assistant professor at Institute of Chemistry, Chinese Academy of Sciences (2013). His research focuses on synthesis and self-assembly of high quality nanomaterials and explore their applications in the fields of biology and energy.

Boyang Zhou is now a PhD candidate at the Institute of Energy Science of Kyoto University. He received his BSc (2010) from Tongji University and Master's degree from China University of Petroleum (Beijing) in 2018. His research focuses on the synthesis of nanomaterials and its application in photovoltaic devices.

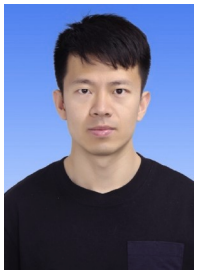

Bowen Guo earned his BSc (2012) at Inner Mongolia University and worked as a technician at Coal-to-liquids (CTL) Chemical Industry of China Energy Investment Corporation (China Energy) for five years. He is a postgraduate student at China University of Petroleum (Beijing). His research focuses on synthesis of two-dimensional materials confining single atoms and explore their applications in the field of new energy.

Peng Gao is an Assistant Professor in the International Center for Quantum Materials and a deputy director of Electron Microscopy Laboratory, Peking University. He received his Bachelor degree of Physics from University of Science and Technology of China in 2005 and Ph.D. degree of Physics in the Institute of Physics, Chinese Academy of Sciences in 2010. Before he joined in Peking University at 2015, he worked in University of Michigan, Brookhaven National Laboratory, and University of Tokyo. His research interests include advanced electron microscopy and spectroscopy, the low dimensional and topological ferroics, and structure and phase transition of energy materials.

Lei Zheng is an associate researcher at the Institute of High Energy Physics, Chinese Academy of Sciences. He received a bachelor's degree in theoretical physics from the Physics Department of Shandong University in 2000. In 2005, he obtained a Ph.D. in optics from IHEP, CAS. His main work focuses on the tender X-ray absorption spectroscopy methodology and X-ray metrology. He is responsible for BSRF's 4B7A tender X-ray beamline, which has attracted a large number of synchrotron users to carry out absorption spectrum measurement research in the energy, materials and environmental fields in this energy region.

Xiaojun Zhang received his BS degree in chemical engineering and technology at the Hunan University in 2016. He is currently a graduate student in the China University of Petroleum (Beijing). His work now focuses on the design of nanomaterials for clean and efficient use of energy.

Shengjie Cui is an Ph.D candidate at the Department of Orthodontics, Peking University School of Stomatology. She received her degree of Stomatology from Peking University in 2017. Her research now focus on the collagen metabolism and the mechanic of nanomaterials.

Hongjun Zhou is the professor of China University of Petroleum (Beijing). He has been the director of Beijing Key Laboratory of High Value Utilization of Biogas since 2005. His research focuses on the development of renewable energy.

Yongsheng Zhou is the professor and President of Peking University School of Stomatology. He also serves as the chairman of Department of Prosthodontics. He achieved his DDS degree in 1994 and PhD in 1998 from Peking University school of Stomatology. He worked as a postdoctoral fellow in University of North Carolina Dental Research Center from 2001 to 2002. His research focuses on material surface modification and bone tissue engineering.

Yan Liu is a professor of Peking University School of Stomatology. She studied as a joint-PhD student at Augusta University from 2009 to 2010, and received her PhD from Huazhong University of Science and Technology in 2011, then joined the faculty at Peking University School of Stomatology in 2011. He also worked as a visiting associated researcher in University of California Los Angeles from 2018 to 2019. Her research focuses on bio-inspired nanomaterials for multifunctional applications.